Synthesis of a Multiple-Model Adaptive Gust Load Alleviation Controller for a Flexible Flutter Demonstrator

Matthias Wüstenhagen, Daniel Ossmann, Charles Poussot-Vassal and Pierre Vuillemin

Today's advanced aircraft designs with respect to new materials and high aspect ratio wings demand for improved control algorithms solving specific issues arising from the new technologies. In this paper a multiple-model adaptive gust load alleviation control system for a highly flexible flutter demonstrator is discussed to solve the issue of increased vulnerability of modern aircraft configurations to gust encounters. Multiple-model adaptive control allows to identify the controller suiting best the aircraft's current mass distribution by means of model detection methods. For a set of discrete mass cases different gust load alleviation controllers are synthesised. The paper presents an innovative control design approach including its verification using a highly flexible flutter demonstrator. Thereby, the advantages and challenges of the multiple-model adaptive control technique in the context of flexible aircraft are discussed.

Synthesis of a Multiple-Model Adaptive Gust Load Alleviation Controller for a Flexible Flutter Demonstrator

Matthias Wüstenhagen*
German Aerospace Center (DLR), 82234 Weßling, Germany

Daniel Ossmann†
Munich University of Applied Sciences, 80335 Munich, Germany

Charles Poussot-Vassal‡ and Pierre Vuillemin§
ONERA - The French Aerospace Lab, 31000 Toulouse, France

Today's advanced aircraft designs with respect to new materials and high aspect ratio wings demand for improved control algorithms solving specific issues arising from the new technologies. In this paper a multiple-model adaptive gust load alleviation control system for a highly flexible flutter demonstrator is discussed to solve the issue of increased vulnerability of modern aircraft configurations to gust encounters. Multiple-model adaptive control allows to identify the controller suiting best the aircraft's current mass distribution by means of model detection methods. For a set of discrete mass cases different gust load alleviation controllers are synthesised. The paper presents an innovative control design approach including its verification using a highly flexible flutter demonstrator. Thereby, the advantages and challenges of the multiple-model adaptive control technique in the context of flexible aircraft are discussed.

I. Introduction

The fuel costs account for the greatest portion of the operating costs of today's aircraft. Therefore, fuel efficiency is one of the most important aspect of new aircraft design concepts [1]. Lightweight wing structures and higher wing aspect ratios hold great potential to increase the fuel efficiency and make flying more economic. However, the wings tend to become more flexible. This makes unstable phenomena like flutter more likely to occur increasing the demand for active flutter suppression (AFS) [2]. Moreover, these aircraft are more vulnerable to manoeuvre and gust loads [3, 4]. Active manoeuvre load alleviation (MLA), like presented in Ref. [5, 6], helps decreasing wing loads during manoeuvres, while gust loads can be reduced by active gust load alleviation (GLA) [7–9]. However, as structurally more efficient aircraft lack a clear separation of rigid body and flexible modes, the synthesis of MLA or GLA controllers is demanding [4].

As part of the Horizon 2020 project *Flight Phase Adaptive Aero-Servo-Elastic aircraft Design methods* (FliPASED, `https://cordis.europa.eu/project/id/815058`) structural control systems for flexible aircraft, like active GLA, are developed and tested on the demonstrator aircraft shown in Fig. 1. More information on the modelling, primary

Fig. 1 FliPASED demonstrator aircraft (`https://flexop.eu/`).

and secondary flight control synthesis and flight testing of the demonstrator aircraft can be found in Ref. [10–14].

*Research Fellow, Institute of System Dynamics and Control, Münchener Straße 20, 82234 Weßling
†Professor, Department of Mechanical, Automotive and Aeronautical Engineering, Lotharstraße 34, 80335 Munich, AIAA Member
‡Research Fellow, DTIS, 2 Av. Edouard Belin, 31000 Toulouse
§Research Fellow, DTIS, 2 Av. Edouard Belin, 31000 Toulouse

For the synthesis of a GLA controller aeroelastic models are needed. Often these models are linearised state-space systems defined at specific operating points within the flight envelope [7, 9, 15]. Adaptive control techniques provide the opportunity to adapt the flight controller to the prevailing conditions during the aircraft's operation and ensure optimal performance over a large range of operational conditions [16]. The simplest form of an adaptive controller is gain-scheduling, where a change in parameters, e.g. airspeed, is measured and used to adapt the controller by means of interpolation techniques within a grid of controllers [16]. There exists quite a rich literature on gain-scheduling techniques applied to flight control problems [17–19]. It is essential that the parameter used for gain-scheduling is directly measurable. However, there also exist variations in the system dynamics due to parameters which cannot be easily measured. An important example is the mass distribution which changes during the mission as the fuel level decreases. Especially, when tanks are located in the wings, a variation of the flexible mode shapes is the consequence [20]. Besides the mass distribution deviations could also be provoked by uncertainties due to unmodelled dynamics or non-linearities in aerodynamic parameters, mass, damping and stiffness matrices and many more. In any of the mentioned cases it is necessary to somehow estimate the system behaviour. Indirect adaptive control offers the opportunity to estimate the current plant parameters with respect to the onboard measurements. Changes in the identified parameters then lead to an update of the controller gains. For the estimation of the plant parameters, however, it is difficult to guarantee that the excitation of the system is rich enough in its spectrum and that the parameters will eventually converge [16]. Direct adaptive control uses a single reference model providing the desired system outcomes. The difference with the real system measurements yields a residual used for control gain update [16]. A major limitation of this approach is its sensitivity to process and sensor noise in the presence of unmodelled dynamics [21]. Due to the limitations of the discussed approaches, in this paper multiple-model adaptive control (MMAC) is used. The idea is to identify the model, among a predefined set of models, that describes the plant behaviour best and switch to the corresponding controller. Generally, there exist several scientific studies on the MMAC, see, e.g. Ref. [16, 20, 22–24]. Ref. [20] proposes model detection filters (MDFs) based on fault detection techniques to identify the best fitting model, as they possess a much smaller order compared to, e.g. Kalman filters. In this paper the method of Ref. [20] is applied to the demonstrator aircraft of the FliPASED project for a GLA controller. Masses are artificially attached in a dedicated modelling process to the structural wing model in order to generate a significant variation in the flexible modes. For each mass case a GLA controller and a MDF are synthesised. A switching logic then selects the most suitable controller based on the aircraft's current mass condition.

The aeroelastic modelling process is described in section II. The definition of the model detection system for models featuring different wing mass distributions is depicted in section III. Subsequently, the model detection algorithm is tested in a simulation. Section IV then summarises the synthesis of the GLA controllers.

II. Control-Oriented Modelling

The aeroservoelastic model is built of the sub-models depicted in Fig. 2. The coupling of the aerodynamics and structural dynamics is the core element. Adding actuators, sensors and the flight controller completes the aeroservoelastic model. In the following, the structural dynamics and the aerodynamics are described further.

A. Structural Dynamics

The rigid and flexible body motion contribute to the structural dynamics. The manoeuvre characteristics of the aircraft are described by the rigid body motion. The flexible body dynamics represent the motion of the flexible aircraft structure. On the one hand the rigid body dynamics are non-linear, while on the other hand the flexible body dynamics are defined linearly. A finite element (FE) model forms the basis of the aircraft structural model, which is reduced with the Guyan reduction [26, 27]. The resulting structural grid model is presented in Fig. 3 as red points. Subsequently, the equations of motion (EOMs) are applied to the structural grid.

1. Equations of Motion

Prior to the application of the EOMs, the following assumptions are made [26]:

1) The earth rotation is neglected, which is why the inertial reference system is earth fixed [28].
2) Over the entire airframe gravity is constant [29].
3) Only small deformations of the airframe are considered which allows the use of linear elastic theory [28].
4) In consequence of the small deformations, the mass moment of inertia J_b remains unchanged [28].
5) Furthermore, loads act on the undeformed airframe [29].

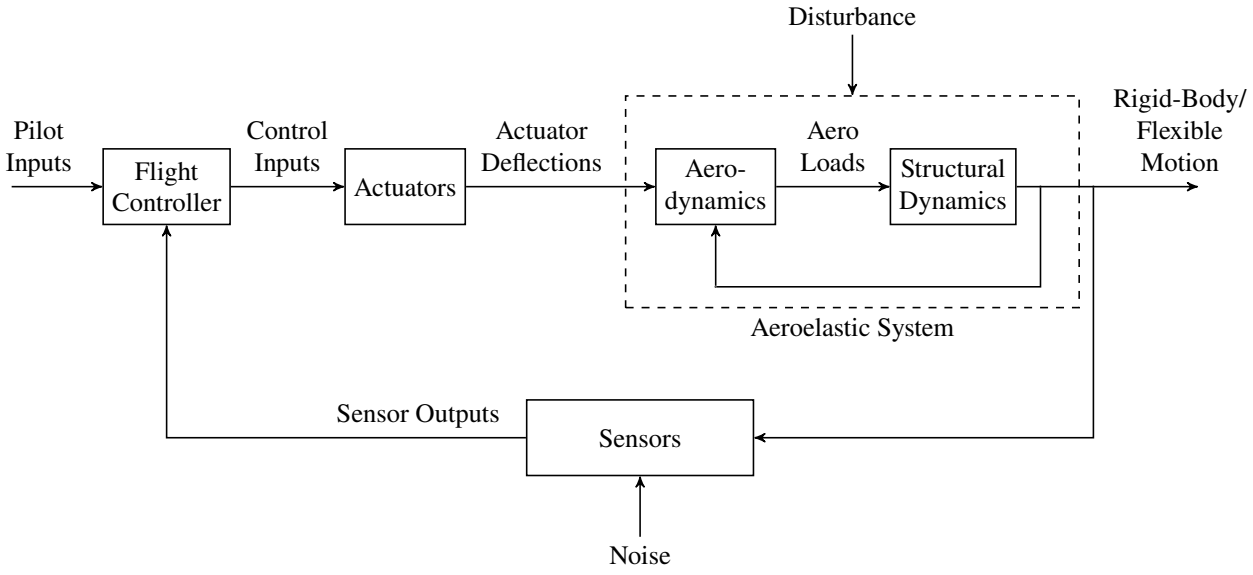

Fig. 2 Aeroservoelastic system [25, 26].

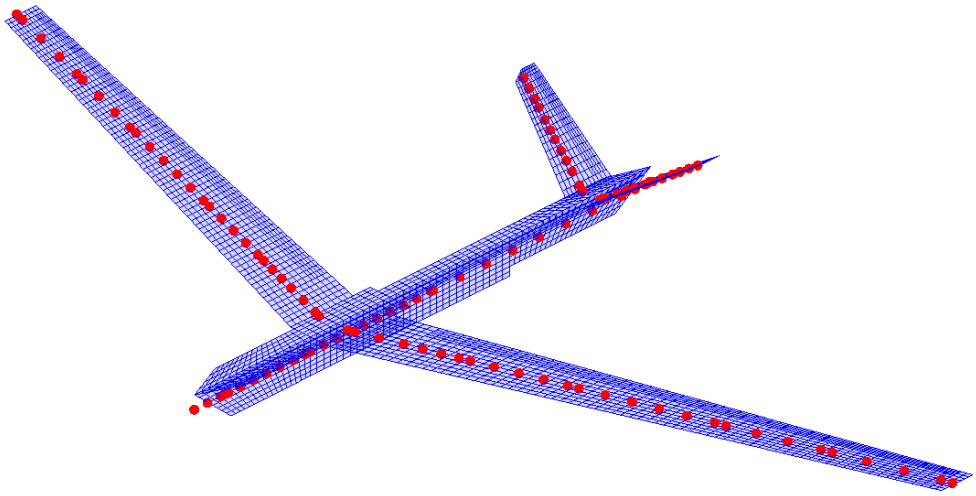

Fig. 3 Structural grid and aerodynamic panels of the demonstrator aircraft.

6) Modal analysis provides orthogonal eigenvectors, which is why the total structural deformation is a linear combination of the modal deflections [29].
7) The rigid body and flexible body EOMs are decoupled [29].

Based on these assumptions the EOMs are defined. They rest upon an equilibrium of forces and moments. The aircraft reacts to the external loads

$$P_g^{\text{ext}} = P_g^{\text{eng}} + P_g^{\text{aero}}, \tag{1}$$

where the thrust and aerodynamic loads are given by P_g^{eng} and P_g^{aero}.

2. Rigid Body Dynamics

For the non-linear flight mechanical EOMs the aircraft is assumed to be a rigid body with constant mass m_b and constant mass moment of inertia J_b. Then the aircraft rigid body motion results from the Newton-Euler EOM [30]

$$\begin{bmatrix} m_b(\dot{V}_b + \Omega_b \times V_b - T_{be} g_e) \\ J_b \dot{\Omega}_b + \Omega_b \times (J_b \Omega_b) \end{bmatrix} = \underbrace{\Phi_{gb}^T P_g^{\text{ext}}}_{P_b^{\text{ext}}} = \begin{bmatrix} F \\ M \end{bmatrix}. \tag{2}$$

The translational and angular velocities of the aircraft are given by V_b and Ω_b for the body frame of reference. The vector g_e is the gravitational acceleration transformed by T_{be} from the earth fixed to the body fixed frame of reference. The loads P_g^{ext} are multiplied with matrix Φ_{gb}^T to the rigid body frame [26, 28].

3. Flexible Body Dynamics

For the flexible motion of the aircraft structure linear elastic theory is applied. The correlation between external loads P_g^{ext} and generalised coordinates u_f, which represent the modal deformation of the structure, yields

$$M_{ff} \ddot{u}_f + B_{ff} \dot{u}_f + K_{ff} u_f = \underbrace{\Phi_{gf}^T P_g^{\text{ext}}(t)}_{P_f^{\text{ext}}(t)}, \tag{3}$$

where the modal mass, damping and stiffness matrices are M_{ff}, B_{ff} and K_{ff}. The modal matrix Φ_{gf} contains the eigenvectors of the structural modes sorted according to their frequency [28]. As typically higher frequency modes contribute less to the flexible body motion, modal truncation is applied to reduce the degrees of freedom (DOFs) with respect to the most relevant eigenmodes [26].

B. Aerodynamics

The aerodynamic loads substantially act on the aircraft structure. They are determined with the vortex lattice method (VLM) for steady aerodynamics and the doublet lattice method (DLM) to combine steady and unsteady aerodynamic effects based on a panel model.

1. Panel Model

The lifting surfaces of the demonstrator aircraft are discretised by the trapezoidal-shaped panels or aerodynamic boxes shown in Fig. 3. The aerodynamic model of the fuselage is a T-cruciform-shaped panel model. Although this is a simplification, the fuselage aerodynamics are approximated quite accurately with respect to higher-order CFD simulations.

2. Steady Aerodynamics

For the VLM each aerodynamic box of the panel model features a horseshoe vortex at point l on the quarter-chord line as depicted in Fig. 4a. The Helmholtz theorem states, each vortex is shed downstream to infinity at the side edges of each box. For an aerodynamic box the Pistolesi theorem needs to be met, prohibiting a perpendicular flow through the control point j. Then the induced velocity v_j at this point needs to equalise the perpendicular component of the incoming velocity vector U_∞, like shown in Fig. 4b. Using the Biot-Savart law v_j caused by the circulation strengths Γ_j of the horseshoe vortices is given as

$$v_j = A_{jj} \Gamma_j. \tag{4}$$

The matrix A_{jj} contains the contribution of each vortex to all induced velocities v_j. Multiplication of the inverse of A_{jj} with $2/c_j$, where c_j is the chord length of the respective aerodynamic box, yields the aerodynamic influence coefficient (AIC) matrix Q_{jj}. In case of steady aerodynamics Q_{jj} is considered to be constant. Then the pressure coefficients Δc_{pj} of the panels are

$$\Delta c_{pj} = Q_{jj} w_j, \tag{5}$$

where $w_j = v_j / U_\infty$ is the downwash. For small angles of attack α_j the downwash w_j is assumed to be equal α_j, i.e. $w_j = \sin(\alpha_j) \approx \alpha_j$.

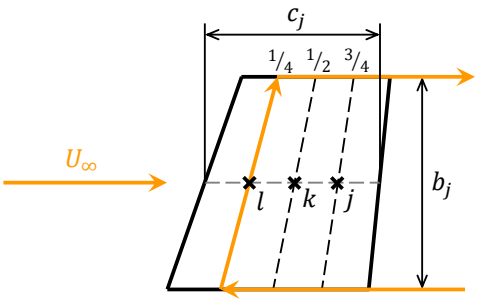

(a) Top view

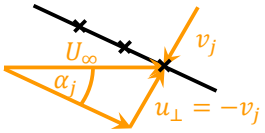

(b) Side view

Fig. 4 Schematic drawing of an aerodynamic box [26].

Various aerodynamic contributions add up to the downwash

$$w_j = w_{j,b_1} + w_{j,\mathrm{cs}_0} + w_{j,\mathrm{cs}_1} + w_{j,f_0} + w_{j,f_1} + w_{j,g_1}. \tag{6}$$

The term w_{j,b_1} depends on the velocity V_b and the angular velocity Ω_b and therefore is a consequence of the aircraft's rigid body motion. The control surface deflections u_{cs} and deflection rates $\dot{u}_{\mathrm{cs}}$ result in w_{j,cs_0} and w_{j,cs_1}. The flexible motion defined by the modal deflection u_f and its derivative $\dot{u}_f$ lead to w_{j,f_0} and w_{j,f_1}. Detailed information on how the contributions are determined is found in Ref. [28]. The contribution w_{j,g_1} is caused by atmospheric turbulence. Within the scope of this paper it is a discrete, vertical 1-cosine gust defined by the gust zone velocity

$$U_{z,\mathrm{gust}}(t) = \begin{cases} \dfrac{U_{\mathrm{gust,max}}}{2}\left(1 - \cos\left(\dfrac{\pi}{H_{\mathrm{gust}}} U_\infty t\right)\right), & \text{if } t_{z,1} \le t \le t_{z,\mathrm{end}} \\ 0, & \text{otherwise,} \end{cases} \tag{7}$$

where $U_{\mathrm{gust,max}}$ is the maximum gust velocity and H_{gust} the gust half length [31]. The gust is stationary in space and with increasing time t the aircraft moves through the gust from nose to aft, like shown in Fig. 5. The gust reaches the

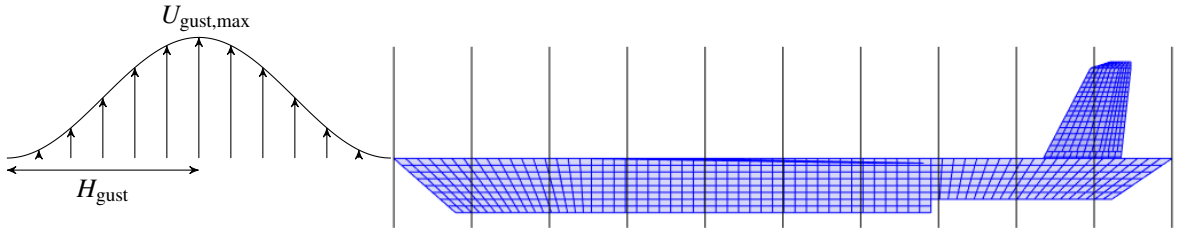

Fig. 5 1-cosine gust and aircraft gust zones.

centre of a gust zone, depicted as a region between two vertical lines of the panel model, at time $t_{z,1}$ and leaves it at time $t_{z,\mathrm{end}}$. All aerodynamic panels within a gust zone are affected by the gust velocity observed at the centre. Namely, within a gust zone the gust velocity is constant. This approach is an approximation which saves a lot of computation time, as it groups many aerodynamic panels into few zones. Furthermore, with ten gust zones it is an accurate enough

implementation for the demonstrator aircraft [32]. The difference in the gust zone velocity of two neighbouring gust zones is caused by a time delay. The transfer function of a time delay is defined by

$$G_{z,\text{delay}}(s) = e^{-t_{z,\text{delay}}s}, \tag{8}$$

where $t_{z,\text{delay}}$ is the time delay in seconds and s is the Laplace variable [32]. In order to be able to convert Equation (8) into a state-space format it is approximated by the second-order Padé approximation [33]

$$G_{z,\text{delay}}(s) \approx \frac{s^2 - \frac{6}{t_{z,\text{delay}}}s + \frac{12}{t_{z,\text{delay}}^2}}{s^2 + \frac{6}{t_{z,\text{delay}}}s + \frac{12}{t_{z,\text{delay}}^2}}. \tag{9}$$

3. Unsteady Aerodynamics

Through the application of the DLM unsteady aerodynamic effects are taken into account. An aerofoil which is suddenly moved forward at an angle of attack creates circulation. As the total circulation has to stay constant according to the Helmholtz theorem, a vortex of the same strength but switched sign is shed from the trailing edge. As it moves downstream it loses its influence on the aerofoil. With increasing time the flow converges to the steady condition. This lag behaviour is caused by unsteady aerodynamics [34]. Unsteady aerodynamics are applied to the panel model by replacing the vortices at the quarter-chord line with doublets. The pressure coefficient then is

$$\Delta c_{pj}(k) = Q_{jj}(k) w_j(k) \tag{10}$$

in the reduced frequency domain, where the reduced frequency k is

$$k = \omega \frac{c_r}{2U_\infty}. \tag{11}$$

In Equation (11) ω depicts the frequency. When $k = 0$ the pressure coefficient $\Delta c_{pj}(k = 0)$ represents the quasi-steady solution. For a transformation of the unsteady aerodynamics to the time domain $Q_{jj}(k)$ is approximated by a rational function approximation (RFA) with Roger's method [35]. The pressure coefficient then is

$$\Delta c_{pj}(k) = \underbrace{Q_{0,jj} w_j(k)}_{\text{quasi-steady}} + \underbrace{\left(Q_{1,jj} + \sum_{i=1}^{n_p} Q_{L_i,jj} \frac{I}{s^\star + p_i} \right) s^\star w_j(k)}_{\text{unsteady}}, \tag{12}$$

where $s^\star$ depicts an equivalent of the Laplace variable for the reduced frequency k. When Equation (12) is transformed to the time domain, additional, so-called lag states x_L are introduced representing the lagging behaviour of the unsteady aerodynamics [26, 28]. Solely due to this kind of approximation the order of the system is enlarged.

C. Integrated Model

As stated in Fig. 2 the structural dynamics are affected by the aerodynamic loads P_g^{aero}. These are

$$P_g^{\text{aero}} = q_\infty T_{kg}^T S_{kj} Q_{jj} w_j + q_\infty T_{ag}^T S_r c_D, \tag{13}$$

where the first term depends on the downwash w_j while the second term depends on the aerodynamic drag loads with reference area S_r and the transformation matrix from the mean aerodynamic centre to the structural grid T_{ag}^T. Matrix S_{kj} depicts an integration relating the pressure in the aerodynamic boxes at point j with the forces at the aerodynamic grid points k. The forces at the grid points k of the aerodynamic boxes are then interpolated onto the structural grid points via the transpose of the spline matrix T_{kg}. Multiplication with the dynamic pressure q_∞ results in the aerodynamic loads. They cause a rigid and flexible body motions of the aircraft structure which, in turn, affects the aerodynamics [25, 26, 28].

The aeroelastic model is extended by second-order transfer functions describing the actuator dynamics of the control surfaces and the engine dynamics. The outputs y of the aircraft model comprise the onboard measurements of an airdata

probe at the nose, the inertial measurement units (IMUs) in the fuselage and the wings as well as the estimated wing root bending moment (WRBM). Finally, the aircraft model can be described by

$$\begin{aligned} \dot{x} &= f(x, u, d) \\ y &= g(x, u) \end{aligned} \tag{14}$$

as a state-space model, where the states, inputs and disturbance are $x = [V_b, \Omega_b, u_f, \dot{u}_f, u_{\text{cs}}, \dot{u}_{\text{cs}}, x_L, ...]^T$, $u = [u_{\text{cs,cmd}}, \delta_{\text{throttle}}]^T$ and $d = d_{\text{gust}}$. The command to the control surface actuators and engine are defined by $u_{\text{cs,cmd}}$ and δ_{throttle}, while the gust disturbance is d_{gust}. Equation (14) describes a non-linear state-space model. For the synthesis of MDFs and GLA controllers it is linearised leading to a set of linear time invariant (LTI) models.

D. Mass Cases for GLA with MMAC

Three different mass cases are artificially created with respect to the MMAC approach for GLA control by loading the most outer structural grid point of each wing with an additional point mass of 450 g, 300 g and 150 g respectively. Table 1 summarises the different mass cases. They are sorted from high to low mass depicting a weight loss as it

Model	Wing Tip Mass
1	450 g
2	300 g
3	150 g

Table 1 Mass cases.

happens due to fuel consumption. The non-linear aeroservoelastic model is built with the three different structural models and linearised subsequently. This is the basis for the synthesis of MDFs and GLA controllers. Masses are artificially attached to the structural model and the aeroelastic open-loop model is linearised for different mass cases.

III. Model Detection System

The MMAC system features a model detection system which comprises residual filters inspired by fault detection algorithms, residual evaluators and the switching logic. Task of the model detection system is to detect and switch to the model matching the current plant behaviour best.

A. Theory

It is assumed that the dynamics of the set of N models is given in the Laplace space by the multiple LTI plant model

$$y_j(s) = G_j(s)u(s) + G_{d,j}(s)d(s),\ j = 1, ..., N, \tag{15}$$

where $y_j(s)$ represents the Laplace transformed output vector, $u(s)$ the Laplace transformed input vector, $d(s)$ the Laplace transformed disturbance input and $G_j(s)$ and $G_{d,j}(s)$ represent the control input to output and the disturbance input to output transfer function matrices, respectively [36].

The basic idea of model detection is depcited in Fig. 6. The aircraft is affected by d and a time-varying parameter $p(t)$. The inputs u and outputs y of the plant are provided to the model detection system. For each model i a residual generation filter Q_i is defined, which then determines a residual r_i. The residual evaluator approximates the signal energy $r_{e,i}$ of the residual r_i, e.g. via a norm computation. The decision which model is judged to be the most valid one is taken by the lowest energy in the residuals. In words, the lowest energy in the residuals simply indicates the model with the lowest distance of all models to the currently active one.

The required residual filters Q_i relate the actual system inputs u and outputs y to the residuals r_i based on the i^{th} system model. It therefore holds

$$r_i(s) = Q_i(s) \begin{bmatrix} y_j(s) \\ u(s) \end{bmatrix},\ i = 1, ..., N, \tag{16}$$

where $r_i(s)$ is the Laplace transformed residual of the i^{th} model detection filter $Q_i(s)$. Note that Equation (16) is the internal form of the i^{th} filter driven by the j^{th} model from the multiple plant model in Equation (15). By inserting the set

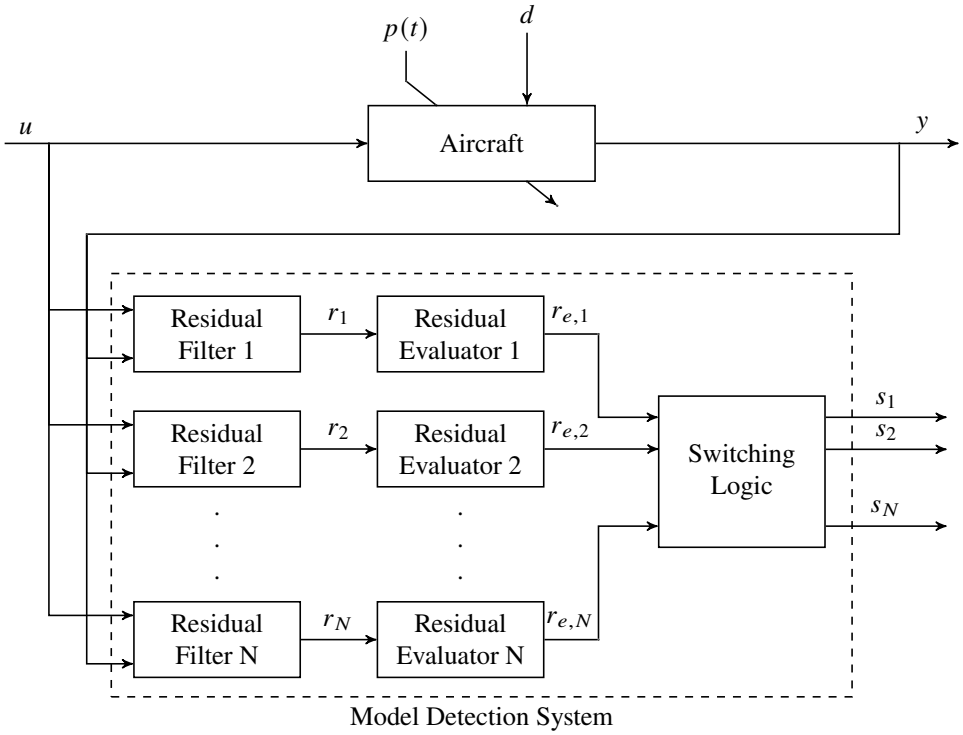

Fig. 6 Model detection procedure [36].

of models from Equation (15) into the set of residual filters Equation (16) leads to

$$\tilde{r}_{ij}(s) = R_{ij}(s) \begin{bmatrix} u(s) \\ d(s) \end{bmatrix} = Q_i(s) \begin{bmatrix} G_j(s) & G_{d,j}(s) \\ I_u & 0 \end{bmatrix} \begin{bmatrix} u(s) \\ d(s) \end{bmatrix}. \tag{17}$$

The matrix I_u represents a unity matrix of the size of $u(s)$ [36]. Based on this internal filter form the model detection problem can be defined as follows:
For the multiple LTI system

$$y_j(s) = G_j(s)u(s) + G_{d,j}(s)d(s),\ j = 1, ..., N, \tag{18}$$

determine N stable filters $Q_i(s),\ i = 1, ..., N$, such that

$$(i)\ [R_{u,ij}(s)\ R_{d,ij}(s)] = 0,\ \forall j = i$$
$$(ii)\ R_{u,ij}(s) \neq 0,\ \forall j \neq i, \text{ and } [R_{u,ij}(s)R_{d,ij}(s)] \text{ stable.}$$

The solvability conditions of this problem can be found in Ref. [36]. Also, Ref. [36] presents adequate numerical tools to solve the problem which are used in this paper. The residual evaluators assess the residuals r_i based on the performance index

$$r_{e,i}(t) = \alpha r_i^2(t) + \beta \int_0^t e^{-\lambda(t-\tau)} r_i^2(\tau) d\tau,\ \alpha \geq 0, \beta > 0, \lambda > 0, \tag{19}$$

which can be interpreted as an energy measure for the residuals. The first term weighs the current squared value of the residual r_i with a factor α, while the second term evaluates its past development multiplied by β. The forgetting factor λ defines how far back in time values of r_i^2 are of importance [23]. A state-space approximation of Equation (19) for all

$r_{e,i}$ assembled in a vector r_e is given in Ref. [20] as

$$\begin{aligned}\dot{x}_e(t) &= \begin{bmatrix} -\lambda_1 & \dots & 0 \\ \vdots & \ddots & \vdots \\ 0 & \dots & -\lambda_N \end{bmatrix} x_e(t) + r^2(t) \\ r_e(t) &= \begin{bmatrix} \beta_1 & \dots & 0 \\ \vdots & \ddots & \vdots \\ 0 & \dots & \beta_N \end{bmatrix} x_e(t) + \begin{bmatrix} \alpha_1 & \dots & 0 \\ \vdots & \ddots & \vdots \\ 0 & \dots & \alpha_N \end{bmatrix} r^2(t). \end{aligned} \tag{20}$$

The vector $r(t)$ includes the residuals $r_i(t)$. The task of the switching logic is to indicate which $r_{e,i}$ is the smallest. It therefore provides a switching index s_i for each $r_{e,i}$ given as

$$s_i = H_{lp}(s) s_i^\star, \tag{21}$$

where $H_{lp}(s)$ represents a second-order low-pass filter to guarantee a smooth transition from one controller to the other, while

$$s_i^\star = \begin{cases} 1, & \text{if } r_{e,i} = \min(r_{e,1}, r_{e,2}, ..., r_{e,N}) \\ 0, & \text{otherwise} \end{cases} \tag{22}$$

indicates the best controller choice.

B. Application and Analysis

The model detection system is implemented and tested for a mutiple LTI model of the demonstrator aircraft defined by the three mentioned mass cases. The control surfaces reacting to the gust encounter are the most outer ailerons on both wings and all four ruddervators of the tail, as shown in Fig. 7. The commanded inputs to these control surfaces

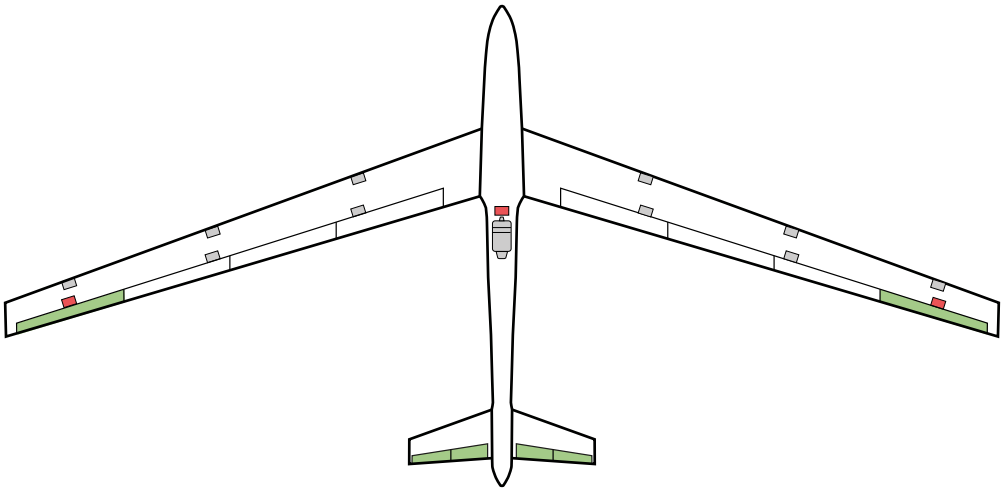

Fig. 7 Demonstrator aircraft with IMUs (red) and control surfaces (green) for GLA control [38].

are allocated in a symmetrical fashion to u_{ail} and u_{rud}. Thus, one deflection signal u_{ail} connected to both ailerons and one deflection signal u_{rud} connected to all four ruddervators are fed to the control surfaces. This combination of signals is valid, as the aircraft is nearly symmetric and only vertical gust encounters are considered. The inputs u_{ail} and u_{rud} are also provided to the MDFs. Furthermore, the pitch angle θ, the pitch rate q_{fu}, the indicated airspeed V_{IAS}, the angle of attack α and the vertical accelerations measured in the fuselage $a_{z,\text{fu}}$ and on both wing tips $a_{z,\text{wtl}}$ and $a_{z,\text{wtr}}$ are the model outputs processed by the MDFs. The position of the vertical acceleration measurements is highlighted in Fig. 7. The disturbance input to the system is d_{gust}. In order to achieve a more convenient numerical conditioning for the synthesis of the MDFs the linearised models are then input-output normalised based on the $\mathcal{H}_\infty$ norm. Balanced reduction techniques are then utilised to decrease the order of the models [37]. In Fig. 8 the comparison

of the poles in the complex plane shows a clear separation between the normalised, reduced models, that are supposed to be distinguishable. By means of the filter synthesis method explained in Ref. [36] three filters Q_i are created. The

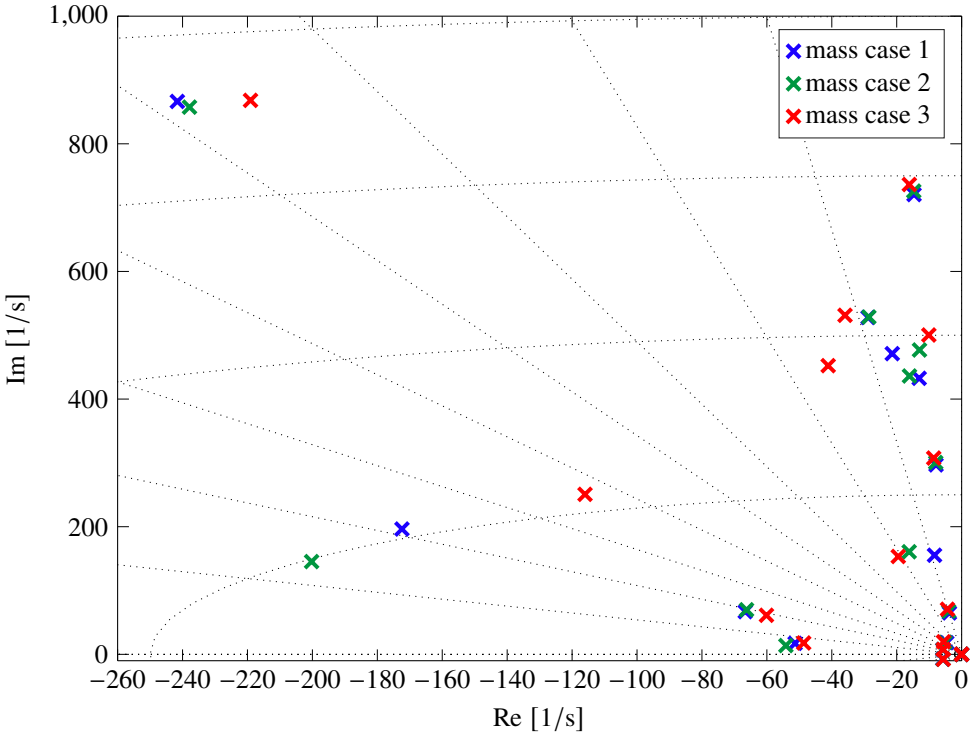

Fig. 8 System poles of the different mass case models.

analysis of $||R_{ij}||_\infty$ in Fig. 9 indicates the maximum distinguishability between the three different mass case models. The x-axis represents the active model, while the y-axis depicts the residuals of the corresponding MDFs. The z-axis indicates the maximum residual value over all frequencies. It is clearly visible that the residuals along the diagonal of the xy-plane are equal to zero, meaning each model is detected by its MDF. Furthermore, a convex shape of $||R_{ij}||_\infty$ is achieved, as the absolute value of the residuals increase the less the active model and the MDF fit together. Also the symmetry condition, which states that

$$||R_{ij}||_\infty = ||R_{ji}||_\infty, \; \forall i \neq j, \tag{23}$$

holds apart from negligible numerical deviations [36]. By means of the synthesised filters three simulations are performed. For each a $1\,^\circ$ step input is given onto u_{ail} after one second. The plant model is considered constant for the entire simulation, i.e $p(t) = \text{const}$. Each simulation is performed with a model corresponding to another mass case. This results in three steady simulations with fixed masses. It is therefore analysed how well the model detection filters, residual evaluators and switching logic perform. The residual evaluators are the same for all model detection filters. The weighting factors of Equation (19) are chosen as $\alpha = 2$ and $\beta = 3$, while the forgetting factors is $\lambda = 0.2$. The switching logic represents a second-order low-pass filter with cut-off frequency $\omega_0 = 1\,\text{rad/s}$ and a critical damping ratio $\zeta = 1$ for a smooth transition. Fig. 10 illustrates how the residuals r_i, the energy in the residuals $r_{e,i}$ and the switching indices s_i evolve for the aforementioned simulations. When looking at the residuals, it is visible that the residual corresponding to the current mass case is the one closest to zero during the entire simulation time. For the first mass case, however, one would expect the residual of the second filter in green to be closer to zero than the residual of the third filter in red. This observation is still subject of current research. The energy in the residuals $r_{e,i}$ are determined like given in Equation (20). In simulation they show that the residual is evaluated within the first few seconds. Therefore, the chosen procedure proves to be appropriate. When looking at the switching indices s_i, it can be seen that for the first mass case model one is selected, i.e. s_1 equals one over the whole simulation time. For mass case 2 and 3, however, the switching index changes from s_1 to s_2 and s_3 respectively. This is due to the fact that the switching mechanism is initialised to point at mass case one at the very beginning of the simulation. As a hard switching should be prevented the aforementioned second-order low-pass filter ensures a smooth transition. Thereby a fading transition between active GLA controllers

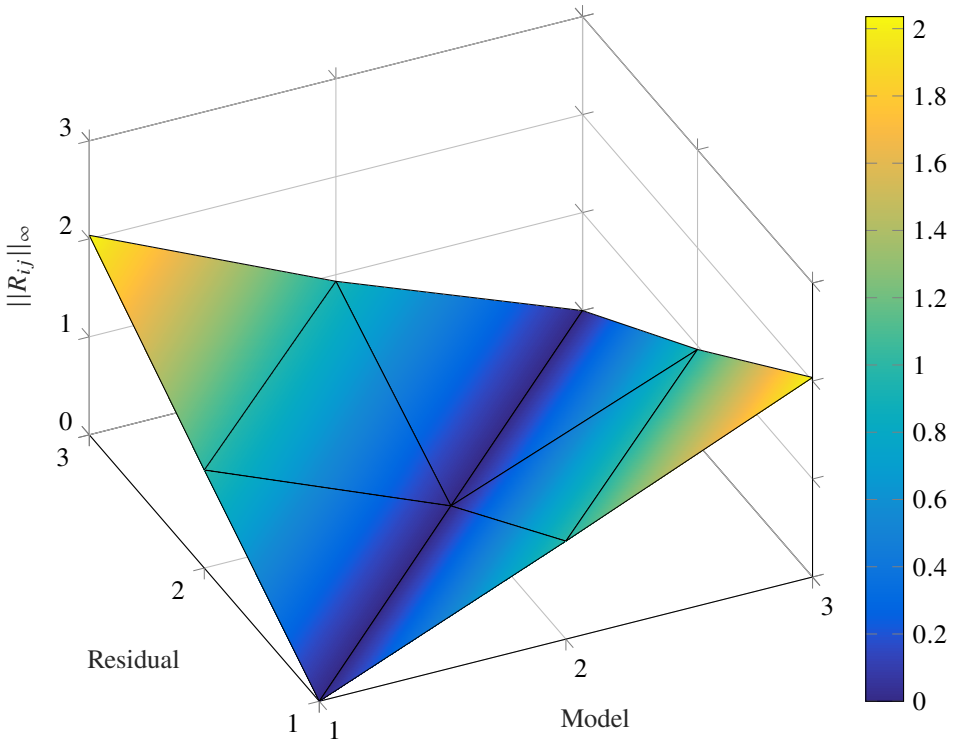

Fig. 9 $\mathcal{H}_\infty$ norm of the residuals for the different models.

can be realised within approximately 10 s. As the changes in mass distribution are thought to happen slowly, this is considered to be an appropriate transition period.

IV. GLA Control Synthesis

The goal of the GLA controller is to reduce the WRBM $M_{x,\mathrm{wro}}$ due to a vertical gust encounter. This should even be possible when the behaviour of the aircraft changes due to variations in the wing mass distribution. Therefore, an appropriate GLA controller is synthesised per mass case.

A. GLA Controller Synthesis Procedure

In the following the GLA synthesis procedure is provided. It is the same for all mass cases. The selected measurements which are fed into the controller are θ, q_{fu}, $a_{z,\mathrm{fu}}$, $a_{z,\mathrm{wtl}}$ and $a_{z,\mathrm{wtr}}$. The controller then generates the commanded deflection signals u_{ail} and u_{rud}. Like for the MDF synthesis, the models are prepared beforehand by normalisation and model order reduction. In the further course of this subsection the aircraft models are assumed to be normalised and reduced.

The controllers are synthesised with the structured $\mathcal{H}_\infty$ method [39]. It generally solves an optimisation problem consisting of N_o equations of the form

$$\min_{K\in\mathcal{K}} ||W_{oi}G_{oi}(K)||_\infty,\ i = 1, ..., N_o, \tag{24}$$

for which the $\mathcal{H}_\infty$ norm of a weighted transfer function $W_{oi}G_{oi}(K)$ is minimised, while the state-space controller K is limited to the parameter space $\mathcal{K}$. The weighting function W_{oi} helps to limit the controller action to certain frequencies. For the GLA controller K_{GLA} the parameter space $\mathcal{K}$ is reduced by the previously selected inputs and outputs and by limiting the number of states to 10. Furthermore, the feedthrough matrix is defined as equal to zero. This demands a roll-off behaviour from the final controller design. The overall control problem for the GLA control is outlined in form of a linear fractional transformation (LFT) in Fig. 11. As can be seen three objectives ($N_o = 3$) are defined [7]:

1) $\min_{K_{\mathrm{GLA}}\in\mathcal{K}} ||W_{o1}G_{\mathrm{CL}}(K_{\mathrm{GLA}})||_\infty$

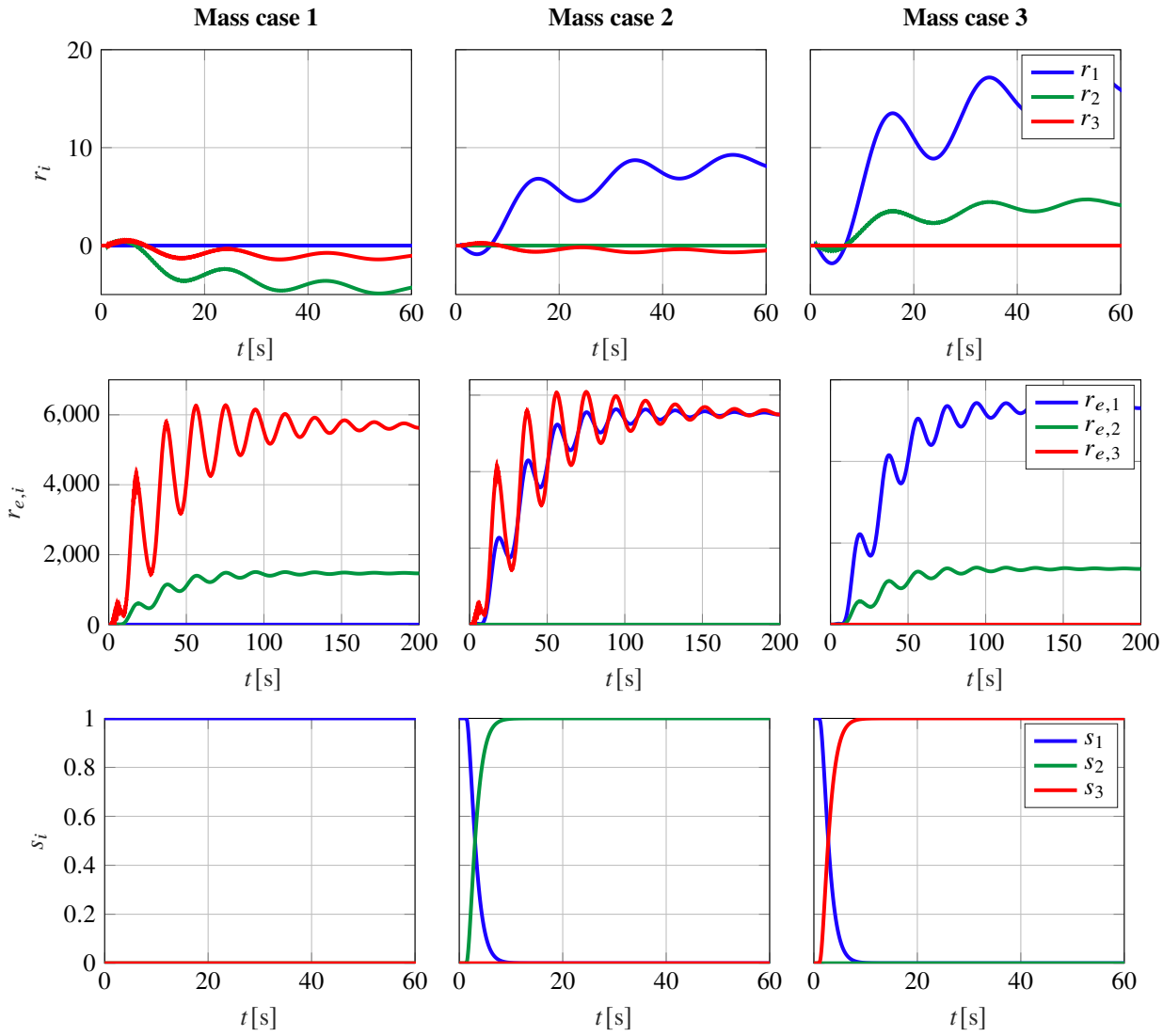

Fig. 10 Residuals, energy in the residuals and switching indices for the different mass cases.

2) $\min_{K_{\mathrm{GLA}} \in \mathcal{K}} ||W_{o2}\,(G_{\mathrm{CL}}(K_{\mathrm{GLA}}) - G_{\mathrm{OL}})\,||_\infty$
3) $\min_{K_{\mathrm{GLA}} \in \mathcal{K}} ||W_{o3} K_{\mathrm{GLA}}||_\infty$

The first objective requests a minimum of the closed-loop transfer function $G_{\mathrm{CL}}(K_{\mathrm{GLA}})$ from disturbance input d_{gust} to WRBM output $M_{x,\mathrm{wro}}$. The weighting function W_{o1} is constant over all frequencies. The second objective focuses on the difference between $G_{\mathrm{CL}}(K_{\mathrm{GLA}})$ and the open-loop transfer function from disturbance input to WRBM output of G_{OL}. The weighting function W_{o2} emphasises a small difference in low frequencies so that the GLA controller does not affect the flight dynamics. Eventually the third objective represents a limitation of the controller K_{GLA} to high frequency inputs. Therefore, W_{o3} rises with increasing frequency. Based on these control objectives a GLA controller is synthesised for each mass case with the optimisation algorithm described in Ref. [40].

In Fig. 12 the open-loop and closed-loop transfer functions from d_{gust} to $M_{x,\mathrm{wro}}$ are shown for all three mass cases. The grey line represents γ_1/W_{o1}, where γ_1 is a measure on how well the first objective is met. For all three mass cases it can be seen that the peak of the WRBM at around 16 rad/s caused by a gust encounter can be significantly reduced. Furthermore, it is visible that the difference between the open-loop and the closed-loop transfer function which is constrained by objective two is small at low frequencies. In high frequencies the open-loop and closed-loop transfer functions also align very well, as the controller action is defined to roll-off by objective three.

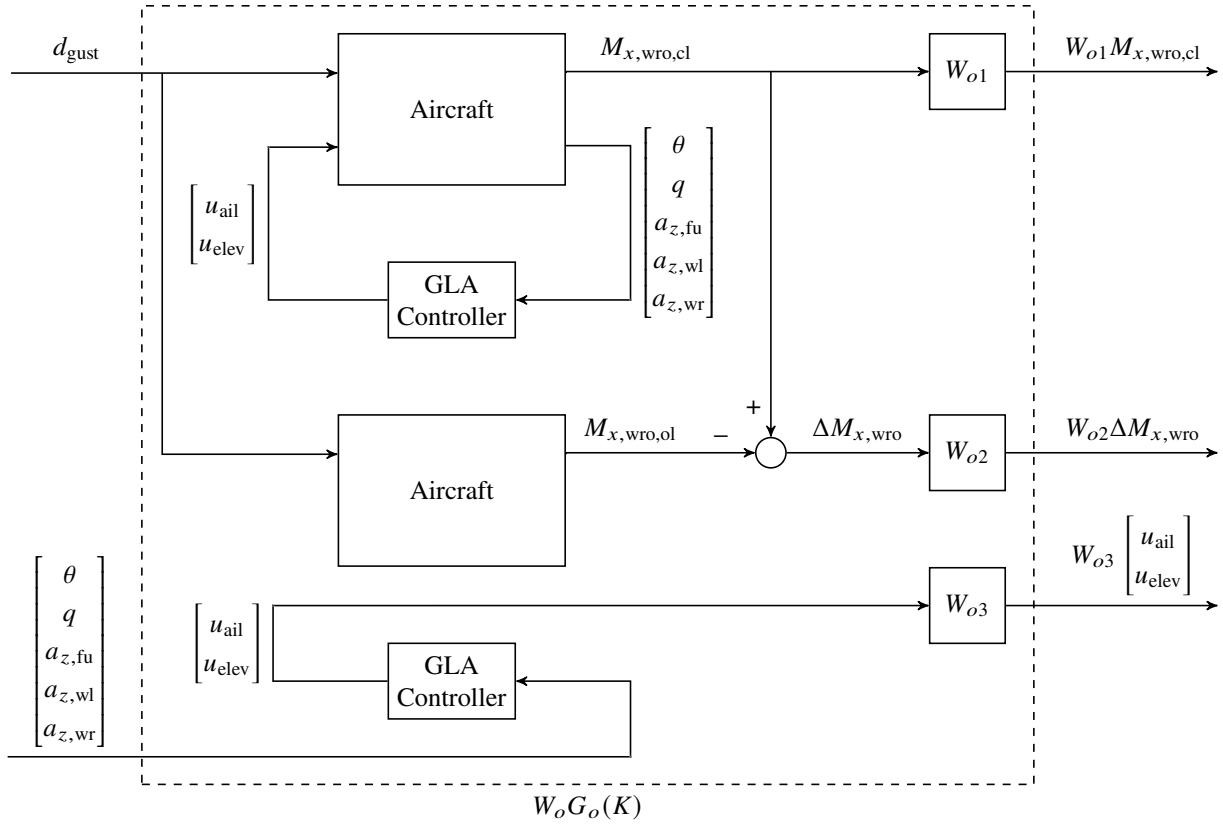

Fig. 11 GLA control problem.

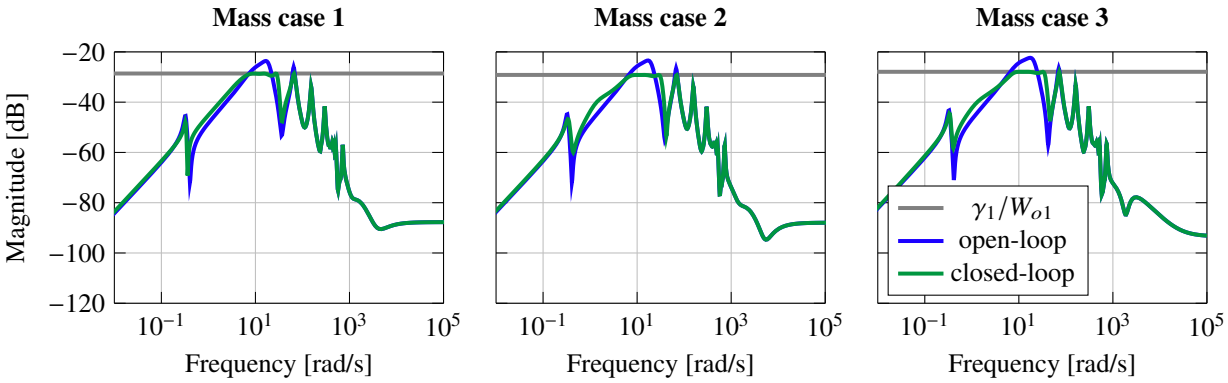

Fig. 12 Transfer function $M_{x,\text{wro}}/d_{\text{gust}}$ for the different mass cases.

B. Closed-Loop Analysis

For the closed-loop analysis the denormalised, full-order system is considered. Time simulations with different gust excitations for the system depicted in Fig. 13 verify that the maximum peak loads of $M_{x,\text{wro}}$ are decreased with the synthesised GLA controllers. Fig. 14 shows the change in the WRBM to ten 1-cosine gust excitations featuring gust half lengths H_{gust} between 4 m and 20 m for the open-loop and closed-loop system. As the reference chord length c_r of the demonstrator aircraft amounts 0.373 m the critical gust half length

$$H_{\text{gust,crit}} = 12.5c_r = 4.66\,\text{m}, \tag{25}$$

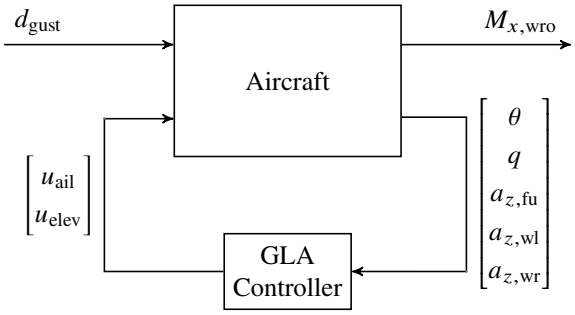

Fig. 13 Closed-loop system including GLA control.

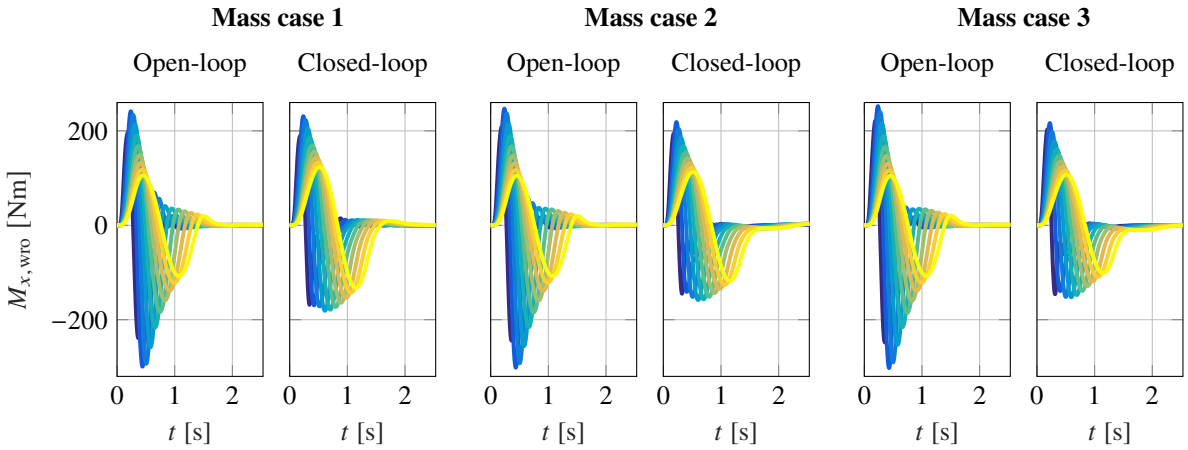

Fig. 14 WRBM in open-loop and closed-loop for different 1-cosine gust half lengths.

defined by Pratt, lies within the considered gust half lengths [41]. From Fig. 14 it is clearly visible, that the maximum peak of the WRBM can be reduced in the closed-loop case for the three mass cases by 4 %, 11 % and 14 %. As can be seen, the greater the mass added to the wing tip, the less the performance improvement with a GLA controller. A further reduction in WRBM could be achieved, when objective two and three are relaxed.

V. Conclusion

For the considered demonstrator aircraft an aeroservoelastic model is developed and utilised for the synthesis of MDFs and GLA controllers. The structural model is based on the Newton-Euler EOM for the rigid body dynamics, while the flexible body dynamics are described by linear elastic theory. The aerodynamics are calculeted with the DLM, while gusts are modelled by a 1-cosine gust that travel over 10 gust zones of the aerodynamic model. Three different mass cases are then generated for which MDFs are synthesised. Simulation shows that the residuals created by the MDFs indicate the correct model. However, so far this has only be shown when the aircraft is exactly represented by one of the mass cases. Intermediate mass conditions or a continuous change in mass have to be further analysed.
The residual evaluation mechanism and the switching logic have proven to be appropriate for the MMAC approach. However, it may be useful to tune the parameters in an automated procedure.
GLA controllers are synthesised with the structured $\mathcal{H}_\infty$ method. In all three mass cases the GLA controllers demonstrate a significant performance improvement with respect to vertical gust encounter. The maximum WRBM could be reduced by at least 4 %.

Further research could include the analysis of the robustness and the performance improvement, like described in Ref. [24], for a MMAC approach for GLA. Also the simulations could involve a non-linear model of the demonstrator aircraft stabilised by primary flight control laws, as shown in Ref. [42–44], to prove the practicality in a more realistic

environment. Finally, the selection and creation of the mass cases could be performed from a more scientific perspective leading to more convenient mass cases for the proposed model detection procedure.

Acknowledgments

The research leading to these results is part of the FLiPASED project. This project has received funding from the European Unions Horizon 2020 research and innovation program under grant agreement No. 815058.

References

[1] International Energy Agency, *Transport, energy and CO_2: Moving toward sustainability*, International Energy Agency, Paris, 2009.

[2] Livne, E., "Aircraft Active Flutter Suppression: State of the Art and Technology Maturation Needs," *Journal of Aircraft*, Vol. 55, No. 1, 2018, pp. 410–452. https://doi.org/10.2514/1.C034442.

[3] Wright, J. R., and Cooper, J. E., *Introduction to Aircraft Aeroelasticity and Loads*, 2nd ed., John Wiley & Sons, Ltd, Chichester UK, 2015.

[4] Regan, C. D., and Jutte, C. V., "Survey of Applications of Active Control Technology for Gust Alleviation and New Challenges for Lighter-weight Aircraft," , No. DFRC-E-DAA-TN4736, 2012. URL https://ntrs.nasa.gov/citations/20120013450.

[5] Burlion, L., Poussot-Vassal, C., Vuillemin, P., Leitner, M., and Kier, T., "Longitudinal Manoeuvre Load Control of a Flexible Large-Scale Aircraft," *Proceedings of the 19th IFAC World Congress 2014*, Vol. 19, edited by E. Boje, 2014, pp. 3413–2418.

[6] Mancini, A., and Vos, R., "The Effect of Maneuver Load Alleviation Strategies on Aircraft Performance Indicators," *AIAA Aviation 2019 Forum*, American Institute of Aeronautics and Astronautics, Reston, Virginia, 2019, p. 3453. https://doi.org/10.2514/6.2019-3272.

[7] Poussot-Vassal, C., Vuillemin, P., Cantinaud, O., and Sève, F., "Interpolatory Methods for Generic BizJet Gust Load Alleviation Function (accepted)," *SIAM Journal on Applied Dynamical Systems*, 2021.

[8] Binder, S., "Simultaneous Optimisation of Composite Wing Structures and Control Systems for Active and Passive Load Alleviation," Dissertation, Delft University of Technology, Delft, 2021. https://doi.org/10.4233/UUID:FAC93CCF-7E0B-4971-A797-D2617E378A1D.

[9] Capello, E., Guglieri, G., and Quagliotti, F., "L1 Adaptive Controller Design for Gust Load Alleviation," *29th Congress of the International Council of the Aeronautical Sciences (ICAS 2014)*, International Council of The Aeronautical Sciences (ICAS), 2014.

[10] Stahl, P., Sendner, F.-M., Hermanutz, A., Rößler, C., and Hornung, M., "Mission and Aircraft Design of FLEXOP Unmanned Flying Demonstrator to Test Flutter Suppression within Visual Line of Sight," *17th AIAA Aviation Technology, Integration, and Operations Conference*, American Institute of Aeronautics and Astronautics, Reston, Virginia, 2017. https://doi.org/10.2514/6.2017-3766.

[11] Rößler, C., Stahl, P., Sendner, F., Hermanutz, A., Köberle, S., Bartasevicius, J., Rozov, V., Breitsamter, C., Hornung, M., Meddaikar, Y. M., Dillinger, J., Sodja, J., de Breuker, R., Koimtzoglou, C., Kotinis, D., and Georgopoulos, P., "Aircraft Design and Testing of FLEXOP Unmanned Flying Demonstrator to Test Load Alleviation and Flutter Suppression of High Aspect Ratio Flexible Wings," *AIAA Scitech 2019 Forum*, American Institute of Aeronautics and Astronautics, Reston, Virginia, 2019. https://doi.org/10.2514/6.2019-1813.

[12] Meddaikar, Y. M., Dillinger, J., Klimmek, T., Krüger, W., Wüstenhagen, M., Kier, T., Hermanutz, A., Hornung, M., Rozov, V., Breitsamter, C., Alderman, J., Takarics, B., and Vanek, B., "Aircraft Aeroservoelastic Modelling of the FLEXOP Unmanned Flying Demonstrator," *AIAA Scitech 2019 Forum*, American Institute of Aeronautics and Astronautics, Reston, Virginia, 2019. https://doi.org/10.2514/6.2019-1815.

[13] Takarics, B., Patartics, B., Luspay, T., Vanek, B., Rößler, C., Bartasevicius, J., Köberle, S., Hornung, M., Teubl, D., Pusch, M., Wüstenhagen, M., Kier, T., Looye, G., Bauer, P., Meddaikar, Y. M., Waitman, S., and Marcos, A., "Active Flutter Mitigation Testing on the FLEXOP Demonstrator Aircraft," *AIAA Scitech 2020 Forum*, American Institute of Aeronautics and Astronautics, Reston, Virginia, 2020. https://doi.org/10.2514/6.2020-1970.

[14] Rößler, C., Bartasevicius, J., Köberle, S., Teubl, D., Hornung, M., Meddaikar, Y. M., Dillinger, J. K., Wüstenhagen, M., Kier, T., Looye, G., Sodja, J., de Breuker, R., Luspay, T., Vanek, B., Georgopoulos, P., and Koimtzoglou, C., "Results of an Aeroelastically Tailored Wing on the FLEXOP Demonstrator Aircraft," *AIAA Scitech 2020 Forum*, American Institute of Aeronautics and Astronautics, Reston, Virginia, 2020. https://doi.org/10.2514/6.2020-1969.

[15] Knoblach, A., *Robust Performance Analysis for Gust Loads Computation: Dissertation*, Verlag Dr. Hut, München, 2015.

[16] Landau, I. D., Lozano, R., M'Saad, M., and Karimi, A., *Adaptive Control*, 2nd ed., Springer London, London, UK, 2011. https://doi.org/10.1007/978-0-85729-664-1.

[17] Lin, Z., "Gain scheduling of aircraft pitch attitude and control of discrete, affine, linear parametrically varying systems," Dissertation, Iowa State University, Ann Arbor, Mi, 2002. https://doi.org/10.31274/rtd-180813-11950.

[18] Aouf, N., Boulet, B., and Botez, R., "A gain scheduling approach for a flexible aircraft," *Proceedings of the 2002 American Control Conference (IEEE Cat. No.CH37301)*, IEEE, 08.05.2002 - 10.05.2002, pp. 4439–4442 vol.6. https://doi.org/10.1109/ACC.2002.1025347.

[19] Fan, W., Liu, H. H. T., and Kwong, R. H. S., "Gain-Scheduling Control of Flexible Aircraft with Actuator Saturation and Stuck Faults," *Journal of Guidance, Control, and Dynamics*, Vol. 40, No. 3, 2017, pp. 510–520. https://doi.org/10.2514/1.G002222.

[20] Ballauf, C., *Dämpfung aeroelastischer Strukturen mit modelladaptiver Regelung: Zugl.: München, Techn. Univ., Diss., 2008*, als ms. gedr ed., Fortschrittberichte VDI Reihe 8, Mess-, Steuerungs- und Regelungstechnik, Vol. 1155, VDI-Verl., Düsseldorf, 2008.

[21] Rohrs, C., Valavani, L., Athans, M., and Stein, G., "Robustness of continuous-time adaptive control algorithms in the presence of unmodeled dynamics," *IEEE Transactions on Automatic Control*, Vol. 30, No. 9, 1985, pp. 881–889. https://doi.org/10.1109/TAC.1985.1104070.

[22] Morse, A. S. (ed.), *Control Using Logic-Based Switching*, Springer London, London, UK, 1997.

[23] Narendra, K. S., and Balakrishnan, J., "Adaptive Control Using Multiple Models," *IEEE Transactions on Automatic Control*, Vol. 42, No. 2, 1997, pp. 171–187.

[24] Fekri, S., Athans, M., and Pascoal, A., "Issues, progress and new results in robust adaptive control," *International Journal of Adaptive Control and Signal Processing*, Vol. 20, No. 10, 2006, pp. 519–579. https://doi.org/10.1002/acs.912.

[25] Tewari, A., *Aeroservoelasticity: Modeling and Control*, Springer New York, New York, NY, 2015. https://doi.org/10.1007/978-1-4939-2368-7.

[26] Wüstenhagen, M., Kier, T., Meddaikar, Y. M., Pusch, M., Ossmann, D., and Hermanutz, A., "Aeroservoelastic Modeling and Analysis of a Highly Flexible Flutter Demonstrator," *2018 Atmospheric Flight Mechanics Conference*, American Institute of Aeronautics and Astronautics, Reston, Virginia, 2018. https://doi.org/10.2514/6.2018-3150.

[27] GUYAN, R. J., "Reduction of stiffness and mass matrices," *AIAA Journal*, Vol. 3, No. 2, 1965, p. 380. https://doi.org/10.2514/3.2874.

[28] Kier, T., and Looye, G., "Unifying Manoeuvre and Gust Loads Analysis Models," *International Forum on Aeroelasticity and Structural Dynamics*, 2009.

[29] Reschke, C., "Integrated Flight Loads Modelling and Analysis for Flexible Transport Aircraft," Dissertation, University of Stuttgart, 2006. https://doi.org/10.18419/opus-3733.

[30] Hofstee, J., Kier, T., Cerulli, C., and Looye, G., "A Variable, Fully Flexible Dynamic Response Tool for Special Investigations (Varloads)," *International Forum on Aeroelasticity and Structural Dynamics*, 2003.

[31] European Aviation Safety Agency, "Certification Specifications for Large Aeroplanes (CS-25)," 2007.

[32] Karpel, M., Moulin, B., and Chen, P. C., "Dynamic Response of Aeroservoelastic Systems to Gust Excitation," *Journal of Aircraft*, Vol. 42, No. 5, 2005, pp. 1264–1272. https://doi.org/10.2514/1.6678.

[33] Hanta, V., and Procházka, A., "Rational Approximation of Time Delay," 2009.

[34] Kier, T., and Hofstee, J., "Varloads - eine Simulationsumgebung zur Lastenberechnung eines voll flexiblen, freifliegenden Flugzeugs," *Deutscher Luft- und Raumfahrtkongress*, 2004.

[35] Roger, K. L., "Airplane Math Modeling Methods for Active Control Design," *AGARD-CP-228*, 1977.

[36] Varga, A., *Solving Fault Diagnosis Problems*, Vol. 84, Springer International Publishing, Cham, 2017. https://doi.org/10.1007/978-3-319-51559-5.

[37] Varga, A., "Balancing Free Square-Root Algorithm for Computing Singular Perturbation Approximations," *30th Conference on Decision and Control*, Vol. 2, 1991, pp. 1062–1065.

[38] Manuel Pusch, *Blending of Inputs and Outputs for Modal Control of Aeroelastic Systems: Dissertation*, Verlag Dr. Hut, München, 2020.

[39] Apkarian, P., and Noll, D., "Nonsmooth H ∞ Synthesis," *IEEE Transactions on Automatic Control*, Vol. 51, No. 1, 2006, pp. 71–86. https://doi.org/10.1109/TAC.2005.860290.

[40] Apkarian, P., Gahinet, P., and Buhr, C., "Multi-model, multi-objective tuning of fixed-structure controllers," *2014 European Control Conference (ECC)*, IEEE, 24.06.2014 - 27.06.2014, pp. 856–861. https://doi.org/10.1109/ECC.2014.6862200.

[41] Pratt, K. G., "A Revised Formula for the Calculation of Gust Loads," 1953.

[42] Luspay, T., Ossmann, D., Wüstenhagen, M., Teubl, D., Baár, T., Pusch, M., Kier, T. M., Waitman, S., Ianelli, A., Marcos, A., Vanek, B., and Lowenberg, M. H., "Flight control design for a highly flexible flutter demonstrator," *AIAA Scitech 2019 Forum*, American Institute of Aeronautics and Astronautics, Reston, Virginia, 2019. https://doi.org/10.2514/6.2019-1817.

[43] Ossmann, D., Luspay, T., and Vanek, B., "Baseline Flight Control System Design for an Unmanned Flutter Demonstrator," *2019 IEEE Aerospace Conference*, IEEE, 02.03.2019 - 09.03.2019. https://doi.org/10.1109/AERO.2019.8741853.

[44] Pusch, M., Ossmann, D., and Luspay, T., "Structured Control Design for a Highly Flexible Flutter Demonstrator," *Aerospace*, Vol. 6, No. 3, 2019, p. 27. https://doi.org/10.3390/aerospace6030027.